Received: 22 June 2017 | Revised: 7 August 2017 | Accepted: 15 August 2017

DOI: 10.1002/er.3867

RESEARCH ARTICLE

WILEY INTERNATIONAL JOURNAL OF ENERGY RESEARCH

Numerical simulation of two-phase cross flow in the gas diffusion layer microstructure of proton exchange membrane fuel cells

Zhiqiang Niu[1] | Kui Jiao[1] | Yun Wang[2] | Qing Du[1] | Yan Yin[1]

[1]State Key Laboratory of Engines, Tianjin University, 135 Yaguan Rd, Tianjin 300350, China

[2]Renewable Energy Resources Lab, Department of Mechanical and Aerospace Engineering, University of California, Irvine, CA 92697-3975, USA

Correspondence
Kui Jiao and Yun Wang, State Key Laboratory of Engines, Tianjin University, 135 Yaguan Rd, Tianjin 300350, China.
Email: kjiao@tju.edu.cn; yunw@uci.edu

Funding information
National Key Research and Development Program of China, Grant/Award Number: 2016YFB0101303

Summary

The cross flow in the under-land gas diffusion layer (GDL) between 2 adjacent channels plays an important role on water transport in proton exchange membrane fuel cell. A 3-dimensional (3D) two-phase model that is based on volume of fluid is developed to study the liquid water-air cross flow within the GDL between 2 adjacent channels. By considering the detailed GDL microstructures, various types of air-water cross flows are investigated by 3D numerical simulation. Liquid water at 4 locations is studied, including droplets at the GDL surface and liquid at the GDL-catalyst layer interface. It is found that the water droplet at the higher-pressure channel corner is easier to be removed by cross flow compared with droplets at other locations. Large pressure difference Δp facilitates the faster water removal from the higher-pressure channel. The contact angle of the GDL fiber is the key parameter that determines the cross flow of the droplet in the higher-pressure channel. It is observed that the droplet in the higher-pressure channel is difficult to flow through the hydrophobic GDL. Numerical simulations are also performed to investigate the water emerging process from different pores of the GDL bottom. It is found that the amount of liquid water removed by cross flow mainly depends on the pore's location, and the water under the land is removed entirely into the lower-pressure channel by cross flow.

KEYWORDS

cross-flow, GDL reconstruction, PEMFC, two-phase, water management

1 | INTRODUCTION

Proton exchange membrane fuel cell (PEMFC) has attracted considerable attentions in a wide range of applications in the past decades because of its outstanding merits such as high efficiency, low operating temperature, and so on. However, the produced liquid water in cathode may block the flow channel and electrode and cause water flooding and performance degradation. Solving water flooding can be achieved by gas flow channel

NOMENCLATURE: D, diameter (m); G, gravity (m s^{-2}); I, index of cell face; K, permeability (m^2); L, GDL cross section length (m); N, number of cell faces; O, geometric center; P, pressure (Pa); T, time (s); U, velocity (m s^{-1}); $\vec{x}$, position (m); Y, y coordinate (m); Z, z coordinate (m) **Greek letters:** α, constant value; ε, porosity; γ, phase fraction; κ, mean curvature; ρ, density (kg m^{-3}); μ, viscosity (kg m^{-1} s^{-1}); θ, contact angle; σ, surface tension coefficient (kg s^{-2}) **Subscripts and superscripts:** A, air; C, capillary; D, dynamic; F, fiber; G, gas; GDL, gas diffusion layer; L, liquid; o geometric center; R, relative; W, water; yz, yz plane

design/optimization, and it has been recognized that serpentine, improved serpentine (such as parallel serpentine), and interdigitated channel designs[1-6] can improve water removal in the channel and gas diffusion layer (GDL), as shown in Figure 1A. One reason is that such designs create in-plane pressure gradients between adjacent gas flow channels, which induce cross flow under the land and hence enhance the reactant convection and water transport efficiency in the GDL,[7-10] as shown in Figure 1B. In this regard, an in-depth understanding of air-water two-phase cross flow between adjacent channels is in need to further optimize the gas flow channel design.

In experiment, various techniques such direct visualization[11,12] and neutron radiography[13] have been conducted to visualize the air-water two-phase cross flow with serpentine flow field. Because the cross flow occurs in the under-land GDL, the detailed GDL structure has significant effects on the behaviors of the two-phase flow. It is difficult to precisely track the air-water cross flow via experimental techniques, which encounter both spatial and time resolution limitation.

In modeling, two-phase flow models can be adopted effectively to investigate the two-phase cross flows in the GDL. The lattice Boltzmann method and finite volume method (FVM) are frequently adopted to study the two-phase flow in the complex structure of GDLs. Tabe et al[14] applied a two-dimensional (2D) lattice Boltzmann method to investigate water behaviors in the GDL and flow channel. Chen et al[15] studied the mass transport and air-water cross flow in the GDL of an interdigitated PEMFC. To take into account the effect of the GDL's microstructure, they reconstructed the 3D GDL through a stochastic method and took a cross section of the reconstructed GDL as the computational domain in their 2D model. As to the FVM method, the volume of fluid (VOF) approach is widely adopted by numerous researchers to investigate the pore-scale two-phase flow in the porous media[16,17] because of its capability of tracking the air/liquid interface.[18] Suresh et al[19] developed a 2D VOF model to investigate the water cross flow in serpentine flow fields. In their study, the GDL structure was simplified as layers of cylindrical fibers that stacked on the top of each other. Park et al[20] conducted a two-phase VOF study to investigate the effect of the fiber hydrophobicity and pressure gradient between the 2 GDL sides on water removal in a 3D-reconstructed GDL. In their study, the GDL structure was modeled by placing 3D cylinders randomly in the in-plane direction. Yin et al[21] used a similar approach to reconstruct a GDL and studied the effect of nonuniform contact angle on the water cross flow.

In the operation of under-land cross flows, the reactant air flows into the GDL from a higher-pressure channel, moves across the under-land GDL region, and gets out of the GDL toward the adjacent lower-pressure channel. Most of previous studies excluded the 2 adjacent channels by considering only the under-land GDL region.[20-23] Moreover, their work only investigated the case where liquid water starts from the GDL-catalyst layer (CL) interface.[14,15,19-21,24,25] The part of two-phase cross flow in the associated gas flow channels was mostly excluded. It is, however, very important to include the gas flow channels that are connected with the under-land GDL to fully understand the water removal due to cross flow, including removal of droplets at the GDL surface.[26]

In this study, a 3D two-phase VOF model is developed in the framework of the FVM to simulate the air-water cross flow between 2 adjacent flow channels, as shown in Figure 1C. To account for the GDL microstructures, the full morphology GDL was reconstructed following the stochastic methods.[15,21,22,27-30] A series of operating parameters, including the droplet location in the higher-pressure channel, pressure difference Δp between 2 adjacent channels, GDL carbon fiber contact angle θ_f, and pore locations at the GDL bottom where water emerges, are investigated. Besides, liquid water may generate at the CL of the cathode and emerge as droplets in the flow channel after flowing through the GDL. When PEMFC works in high temperature, the water vapor at the CL can diffuse into the GDL and flow channel and condenses under the cooling effect of land and walls of flow channel. To simplify the study, the condensation process of water vapor in the GDL and flow channel is not taken into account. In reality, when water emerges from the GDL bottom, the droplet can exit on the GDL surface simultaneously. To investigate the dynamic behaviors of liquid water at the different locations, 2 kinds of assumptions of initial liquid water distribution are considered separately in this study: (i) The water droplet is initially stagnant on the GDL surface and (ii) the liquid water is purged into the GDL from the GDL bottom. The investigation of coupling these 2 kinds of assumptions will be conducted in the future research.

2 | NUMERICAL MODEL

2.1 | Reconstruction of carbon paper gas diffusion layer

Generally, GDL should be porous media that consists of carbon paper or carbon cloth and has complex microstructures.[31,32] For considering the pore-scale cross flow in the GDL, it is necessary to obtain the detailed pore morphology of the GDL. In this study, The GDL is treated as carbon paper and is reconstructed through the stochastic method[15,21,22,27-30] based on the following

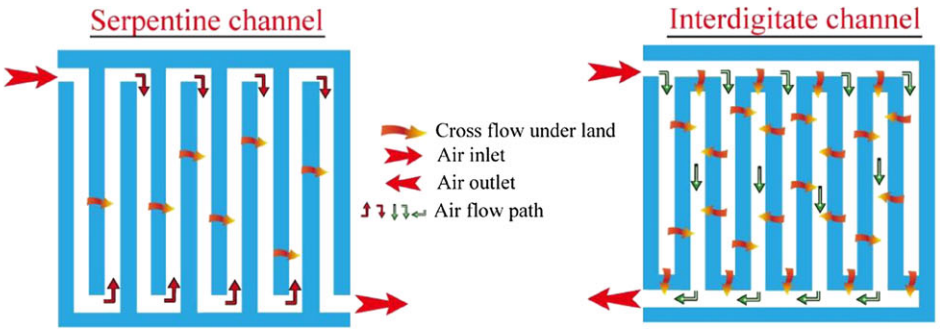

(A)

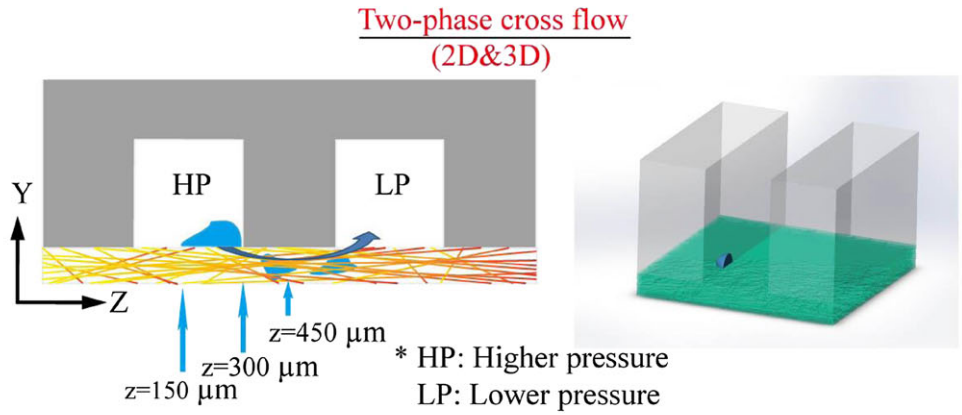

(B)

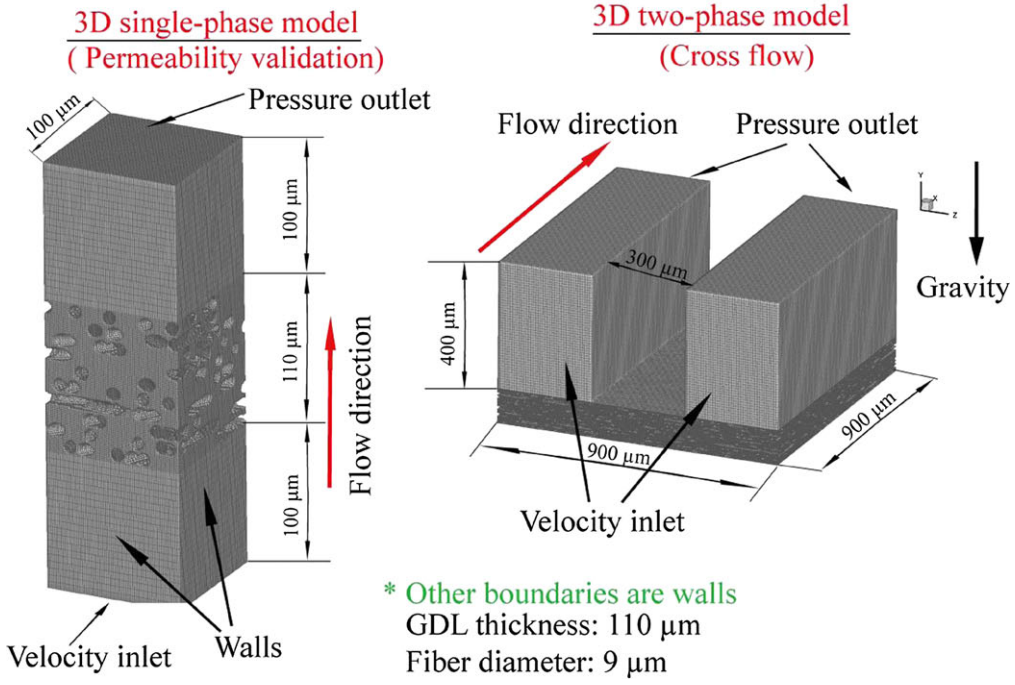

(C)

FIGURE 1 Schematics of two-phase cross flow and numerical model in proton exchange membrane fuel cell (PEMFC). (A) Cross flow in the serpentine and interdigitated flow channel; (B) two-phase cross flow in the under-land gas diffusion layer (GDL); (C) the computational domains and boundary conditions used for the permeability validation and 3D two-phase cross flow numerical simulations [Colour figure can be viewed at wileyonlinelibrary.com]

assumptions: (i) The carbon fibers of the GDL are straight cylinders with same diameter and arranged randomly in a plane; (ii) the orientation of carbon fibers is perpendicular to the GDL thickness direction and allowed to be overlapped; and (iii) the polytetrafluoroethylene treatment is ignored. Figure 1C shows a reconstructed carbon paper GDL of 100 μm × 110 μm × 100 μmwith the porosity of 0.61 and the fiber diameter $d_f = 9$ μm. A detailed permeability validity of the reconstructed GDL is also performed in the section 3.1.

2.2 | Governing equations

In this study, the two-phase laminar flow in the channel and GDL is considered. A modified VOF model is adopted to improve the resolution of the free-phase interface.[33] The governing equations are as follows:

Mass conservation equation:

$$\nabla \cdot \vec{U} = 0 \tag{1}$$

Phase conservation equation:

$$\frac{\partial \gamma}{\partial t} + \nabla \cdot \left(\vec{U}\gamma\right) + \nabla \cdot \left[\vec{U}_r \gamma(1-\gamma)\right] = 0 \tag{2}$$

Momentum conservation equation:

$$\frac{\partial\left(\rho\vec{U}\right)}{\partial t} + \nabla \cdot \left(\rho\vec{U}\vec{U}\right) - \nabla \cdot \left(\mu\nabla\vec{U}\right) - \left(\nabla\vec{U}\right) \cdot \nabla\mu = -\nabla p_d - \vec{g} \cdot \vec{x}\nabla\rho + \sigma\kappa\nabla\gamma \tag{3}$$

where $\vec{U}$ the velocity vector is shared by the 2 phases throughout the flow domain; $\vec{U}_r = \vec{U}_l - \vec{U}_g$ is the relative velocity of liquid and gas at the interface, designated as "compression velocity"; and γ, σ, and κ are the phase fraction, surface tension coefficient, and mean curvature of the phase interface, respectively. The effective density and dynamic viscosity, ρ and μ, are calculated as follows:

$$\rho = \rho_l\gamma + \rho_g(1-\gamma) \tag{4}$$

$$\mu = \mu_l\gamma + \mu_g(1-\gamma) \tag{5}$$

p_d is a modified pressure for simplifying the definition of boundary conditions, which is defined as

$$p_d = p - \rho\vec{g} \cdot \vec{x} \tag{6}$$

where $\vec{x}$ is the position vector.

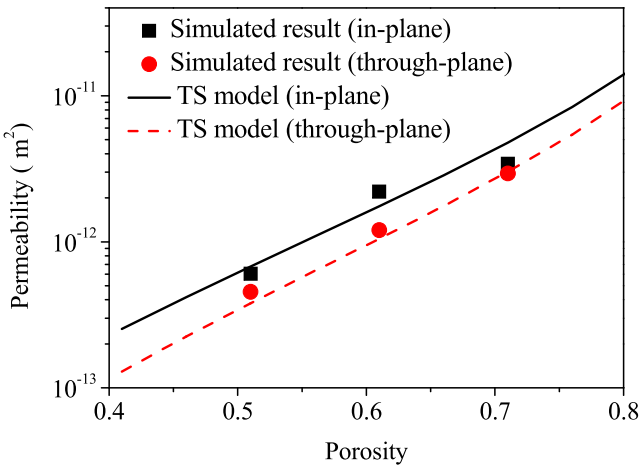

FIGURE 2 Comparison of permeability between the reconstructed gas diffusion layer (GDL) of the present study and Tomadakis-Sotirchos (TS) model in Tomadakis and Robertson[35] (fiber diameter:$d_f = 9$ μm) [Colour figure can be viewed at wileyonlinelibrary.com]

TABLE 1 Simulation cases

Objectives	Operating Parameters	Water Generation Method	Air Inlet Velocity	Pressure Difference	Time Step
Droplet location	Middle ($R_w = 50$ μm) $\theta_f = 90°$ Corner ($R_w = 100$ μm) $\theta_f = 90°$	Initially stagnant droplet	10 m s^{-1}	10 kPa	3×10^{-8} s
Pressure difference	$\theta_f = 90°$	Initially corner stagnant droplet ($R_w = 100$ μm)	10 m s^{-1}	4 kPa 7 kPa 10 kPa	6×10^{-8} s 4×10^{-8} s 3×10^{-8} s
Fiber contact angle	$\theta_f = 90°, 120°$	Initially corner stagnant droplet ($R_w = 100$ μm)	10 m s^{-1}	10 kPa	3×10^{-8} s
	$\theta_f = 90°, 120°$ $z = 300$ μm	Water emerging from the bottom pore of GDL		7 kPa	4×10^{-8} s
Pore location of water emerging	$z = 150, 300, 450$ μm $(\theta_f = 120°)$	Water emerging from the bottom pore of GDL	10 m s^{-1}	7 kPa	4×10^{-8} s

Note: In 2 kinds of water generation methods, the center of initial stagnant droplet/gas diffusion layer (GDL) bottom pore is located at $x = 200$ μm.

2.3 | Initial and boundary conditions

The no-slip conditions are imposed on the sides of the GDL and 2 flow channels. The inlets of 2 adjacent channels are the same fixed velocity inlet, and the constant pressure outlets with different values are imposed on the outlet of these 2 channels. The gravity is set along the negative y-direction. The fiber contact angle of the GDL θ_f ranges from 90° to 120°, and the other walls have the same contact angle of 90°. Two liquid water generation methods (I. Water droplet is initially located at the GDL surface; II. Water emerges from a pore at the GDL bottom) are considered in different cases. For II, the water inlet pore has a dimension of 50 μm × 50 μm. A water inlet velocity of 1 m s^{-1} is set to elucidate the complex two-phase cross flow. The water inlet flow may result from the mode of water eruption in porous media, as observed by Harting et al.[34] The details of the various operating conditions are given in Table 1.

2.4 | Numerical procedures

The detailed dimensions of the computational domains in the present study are shown in Figure 1C. The GDL and flow channel are both discretized with structured mesh. The computational domains contain 1 million and 1.5 million cells for the permeability evaluation and the numerical simulation of two-phase cross flow, respectively. A grid and time-step independency test has been carried out to guarantee the simulation accuracy. All the numerical simulations were performed in a CFD software-Open FOAM. The governing equations were discretized by using the second order scheme. The

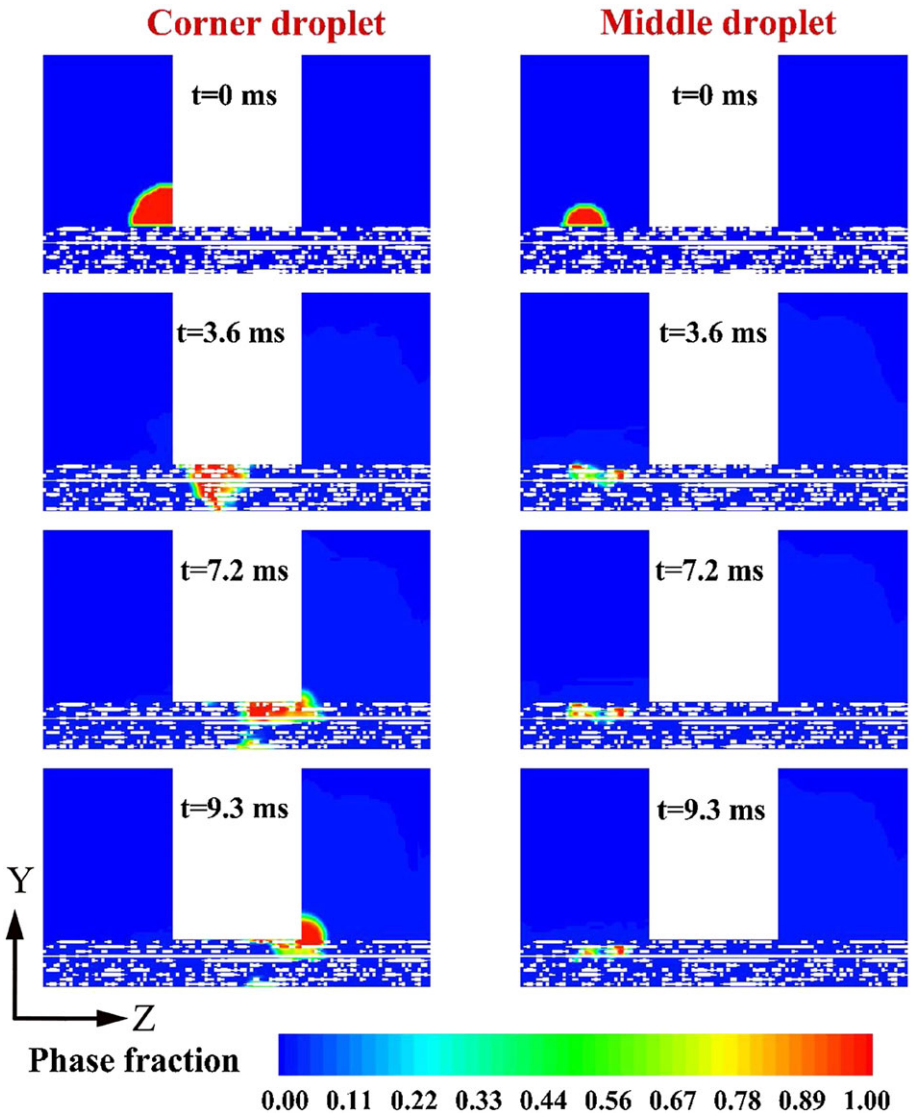

FIGURE 3 Water droplet cross-flow behaviors from the higher-pressure channel to the lower-pressure channel at the slice of $x = 200$ μm (left column: water droplet is initially located at the corner of channel; right column: water droplet is initially located at the middle of channel; operating parameters: $\theta_f = 90°$, $\Delta p = 10$ kPa) [Colour figure can be viewed at wileyonlinelibrary.com]

PIMPLE scheme coupling the semi-implicit method for pressure linked equation scheme and pressure implicit with splitting of operators scheme is responsible for the coupling solution of the pressure and velocity. The parallel approach open-MPI was adopted to accelerate the simulation. A single case took about 30 days by using 12 parallel processors (2.93 GHz and 2 GB memory).

3 | RESULTS AND DISCUSSION

3.1 | Validation of gas diffusion layer permeability

The permeability is a key parameter to evaluate the characteristics of the GDL. In this section, single-phase flow simulation is performed. The in-plane and through-plane permeabilities of the simulated GDL are calculated by Darcy's law:

$$K = \frac{\mu L}{\Delta p} U_{\mathrm{GDL}} \tag{7}$$

where U_{GDL} is the superficial velocity, Δp the pressure difference, L the GDL cross section length, and μ the viscosity. The detailed computational domain and boundary conditions are illustrated in Figure 1C. To validate this model, several GDL samples of different porosity were reconstructed. The results were compared with the below Tomadakis-Sotirchos model (TS model) that is commonly used to estimate the permeability of fibrous porous media:[35]

$$K = \frac{\varepsilon}{32(\ln\varepsilon)^2} \frac{(\varepsilon-\varepsilon_{\mathrm{p}})^{\alpha+2} d_{\mathrm{f}}^2}{(1-\varepsilon_{\mathrm{p}})^{\alpha}\left[(\alpha+1)\varepsilon-\varepsilon_{\mathrm{p}}\right]^2} \tag{8}$$

where ε and d_{f} are the porosity and fiber diameter, respectively; α and ε_{p} are constant determined by the GDL structure and flow direction. In this study, α and ε_{p} are set values as following:

$$\begin{cases} \alpha = 0.521, \varepsilon_{\mathrm{p}} = 0.11 (\text{in-plane flow}) \\ \alpha = 0.785, \varepsilon_{\mathrm{p}} = 0.11 (\text{through-plane flow}) \end{cases} \tag{9}$$

Figure 2 shows the in-plane and through-plane permeabilities of the reconstructed GDL and TS model under various porosities. It is seen that the simulated through-plane permeability agrees well with the TS model. The simulated in-plane permeability has a deviation of 20% from the TS model. This deviation may be due to a small part (in the in-plane direction) of a GDL considered in this study, which may not be representative.

3.2 | Effect of droplet location in flow channel

This section considers liquid water droplet at different locations of the higher-pressure channel. The fiber

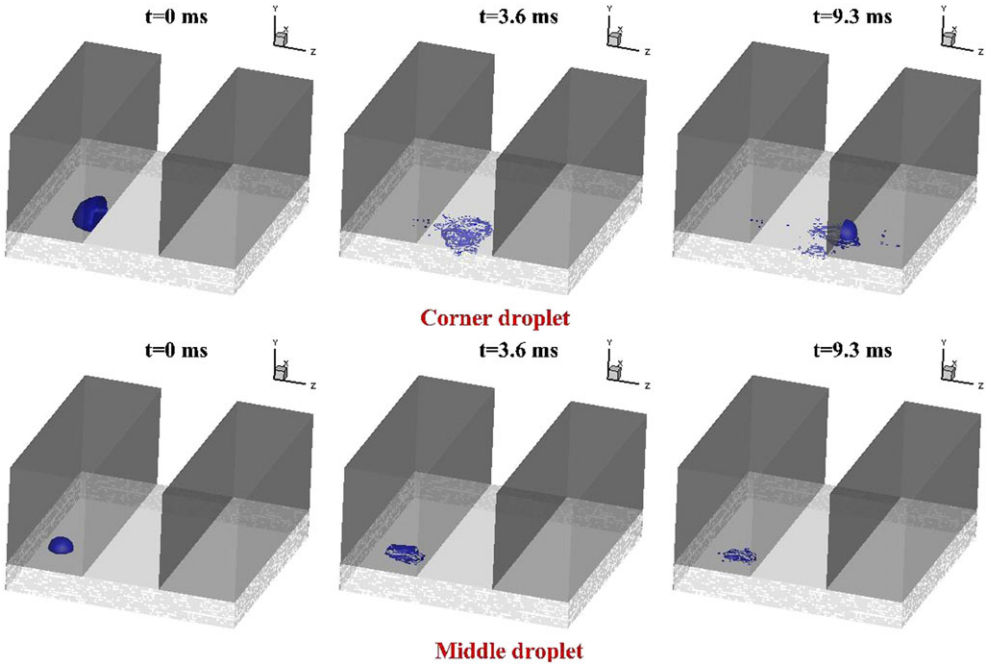

FIGURE 4 Iso-surface of liquid water phase fraction $\gamma = 0.5$ for the droplets with different locations (top: water droplet is initially located at the corner of channel; bottom: water droplet is initially located at the middle of channel; operating parameters: $\theta_{\mathrm{f}} = 90^{\circ}$, $\Delta p = 10$ kPa) [Colour figure can be viewed at wileyonlinelibrary.com]

contact angle is $\theta_f = 90^\circ$. Other operating parameters are listed in Table 1. Droplets at the middle and corner of the higher-pressure channel are studied respectively. Figure 3 shows the two-phase cross flow behaviors for the 2 cases at the slice of $x = 200$ μm. At the initial stage, liquid was forced into the pores of GDL due to the pressure difference for the 2 cases. After that, the middle droplet stops moving and remains stagnant within the upper layer of GDL. As to the corner location, the liquid was forced to enter the under-land GDL and flow to the lower-pressure channel. Figure 4 shows the 3D liquid water behaviors. It can be observed that for the corner droplet case, liquid water flows into the lower-pressure channel via the left corner region. A similar phenomenon was observed in the experiment of the interdigitated cathode flow channel by using in situ neutron radiography (higher-liquid water accumulation at the corner region in the lower-pressure channel).[36]

In addition, the geometric center $\vec{O}$ of the phase fraction iso-surface $\gamma = 0.5$ in Figure 4 was computed to describe the droplet motion trail and shown in Figure 5. The coordinates of $\vec{O}$ are calculated as follows:

$$\vec{O} = \begin{cases} x_o = \frac{1}{N}\sum_{i=1}^{N} x_i \\ y_o = \frac{1}{N}\sum_{i=1}^{N} y_i \\ z_o = \frac{1}{N}\sum_{i=1}^{N} z_i \end{cases} \tag{10}$$

where x_o, y_o, and z_o are the x, y, and z coordinates of geometric center $\vec{O}$; N is the number of cell faces composing phase fraction iso-surface; and i is the index of cell face. The curves of coordinates of geometric center $\vec{O}$ versus time are plotted in Figure 5.

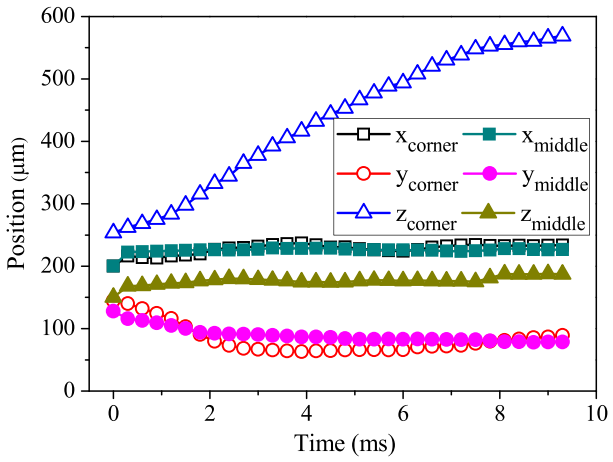

FIGURE 5 Coordinates of the geometric center of water phase iso-surface $\gamma = 0.5$ in the corner and middle droplet cases [Colour figure can be viewed at wileyonlinelibrary.com]

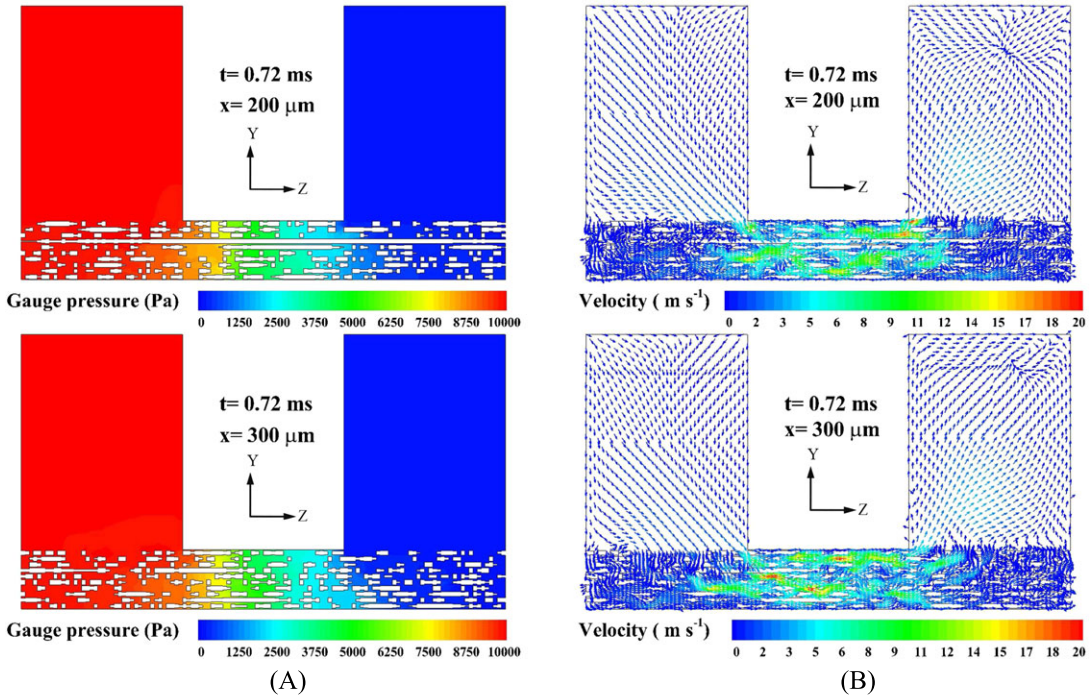

FIGURE 6 Pressure and velocity of cross section distributions on the slice of $x = 200$ μm and $x = 300$ μm at the time instance $t = 0.72$ ms in the middle droplet case. (A) Gauge pressure; (B) velocity vector of cross section. Operating parameters: $\theta_f = 90^\circ$, $\Delta p = 10$ kPa [Colour figure can be viewed at wileyonlinelibrary.com]

The reason causing the middle droplet stagnation in the upper layer of GDL is the small pressure gradient at the middle of higher-pressure channel, which can be observed in Figure 6A. And a small pressure gradient is difficult to drive the middle droplet flow into deep pores of the GDL. Conversely, the big pressure gradient around

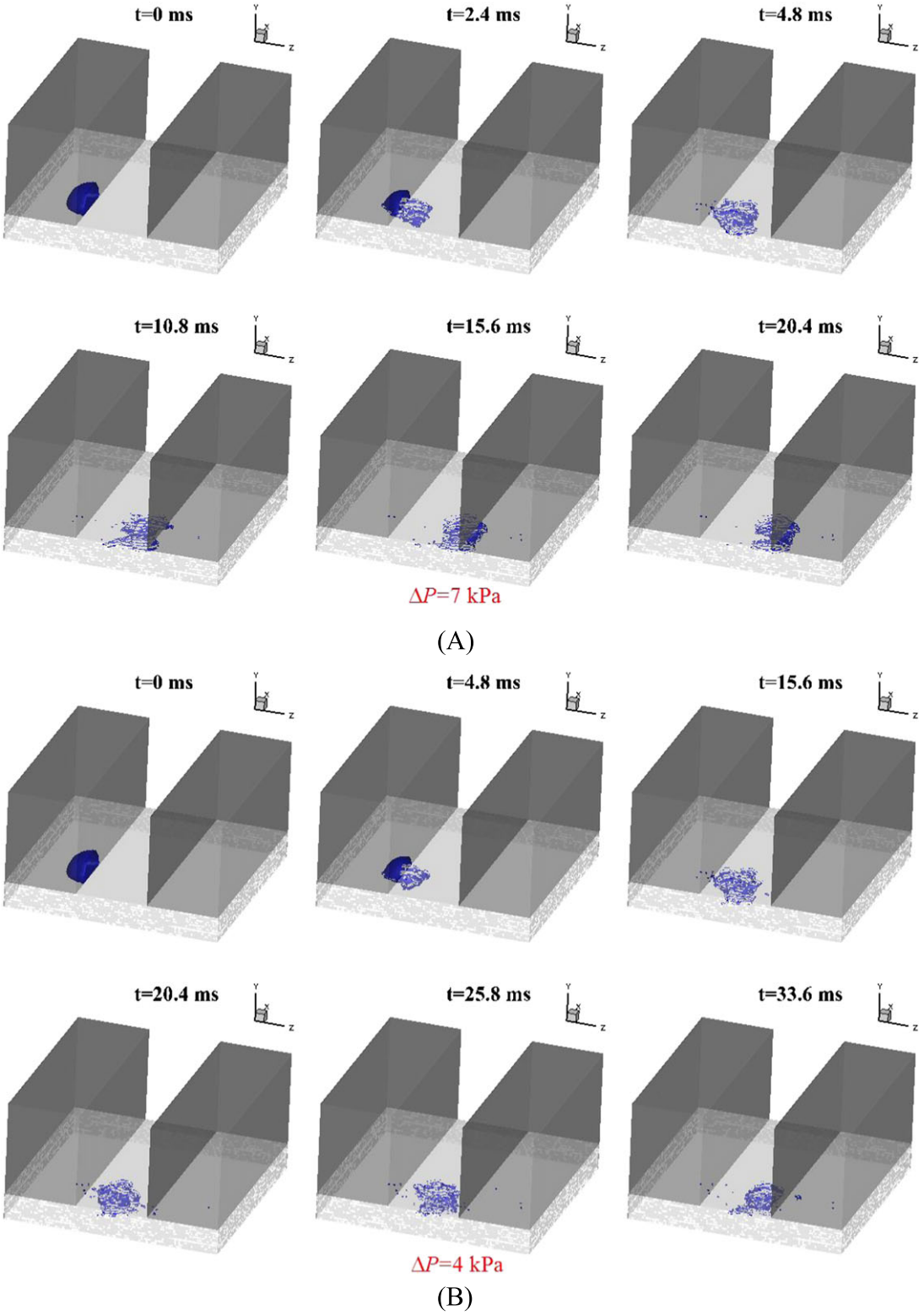

FIGURE 7 Iso-surface of liquid water phase fraction $\gamma = 0.5$ in cases with different Δp. (A) $\Delta p = 7$ kPa, $\theta_f = 90^\circ$; (b) $\Delta p = 4$ kPa, $\theta_f = 90^\circ$ [Colour figure can be viewed at wileyonlinelibrary.com]

the corner of flow channel can overcome the flow resistance in the GDL and push the side droplet into the lower-pressure channel transversely.

Figure 6B shows the cross-section velocity vectors $\overrightarrow{U}_{yz}$ on the slice of $x = 200$ μm and $x = 300$ μm at time instance $t = 0.72$ ms. It is also noted that the main path of the two-phase cross flow is between the adjacent corners of 2 channels and most air and water flows transversely into the lower-pressure channel via its the left corner.

3.3 | Effect of pressure difference Δp

The pressure difference Δp between 2 adjacent channels changes with operating condition and channel configuration.[20,37,38] According to the experiment,[37] for a single serpentine channel, the pressure difference between adjacent channels can be nearly 2 kPa for the cathode air stoichiometry 2.0 when the current density is 0.6 A cm^{-2}. The work[8] also indicated about 1.2 kPa pressure difference in the studied channel configuration. As the length of serpentine channel increases, the maximum pressure difference between adjacent channels will increase. Moreover, the pressure difference between adjacent channels in interdigitated flow field design can be larger than that of serpentine flow field design.[39] In this study, 3 pressure differences Δp (4 kPa, 7 kPa, and 10 kPa) are chosen for a parametric study to illustrate the effect of Δp on the two-phase cross flow behaviors.

Figure 7 shows the phase fraction γ iso-surfaces of side droplet transport process under the Δp of 7 kPa and 4 kPa. It can be observed that the apparent two-phase flow characteristics in the cases with different Δp are similar, but the liquid water cross flow velocity is significantly different. The curves of the z coordinate of the geometric center of phase fraction versus time in Figure 7 are plotted in Figure 8. It is obviously observed that a large Δp has a significant effect on improving the two-phase cross flow velocity. It just takes 9.3 ms for side droplet flowing into lower-pressure channel in the case of $\Delta p = 10$ kPa, while nearly 16 ms and 34 ms are taken for the side droplet arriving at the corner of lower-pressure channel in the cases of $\Delta p = 7$ kPa and $\Delta p = 4$ kPa, respectively.

It can also be noted that the motion velocity of the liquid water becomes slow nearby the corner of lower-pressure channel in the 3 cases. This is because of a small pressure gradient in this region, which can be observed in Figure 6A.

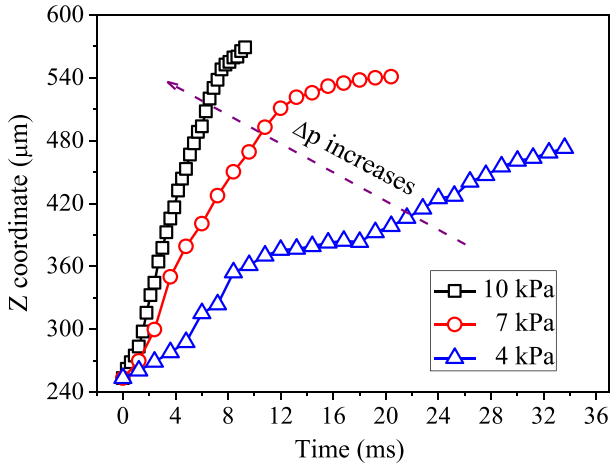

FIGURE 8 z coordinate of geometric center of water phase iso-surface $\gamma = 0.5$ at different time instances for cases with different Δp [Colour figure can be viewed at wileyonlinelibrary.com]

3.4 | Effect of fiber contact angle θ_f

The fiber contact angle θ_f is determined by the polytetrafluoroethylene loading in GDLs. For considering the effects of θ_f on the two-phase cross flow, 2 kinds of fiber contact angles $\theta_f = 90^\circ$ and $\theta_f = 120^\circ$ are investigated, respectively. It is well known that water is generated in the cathode and discharged into the flow channel through the GDL. Two initial locations of liquid water are considered in this section respectively; that is, a droplet is

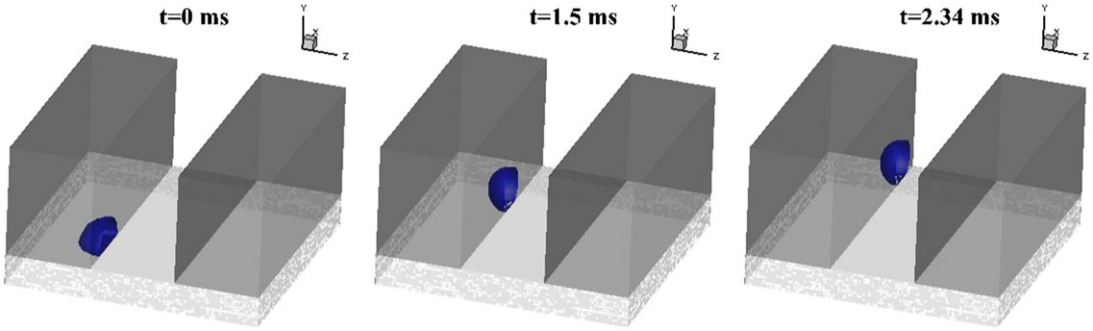

FIGURE 9 Iso-surface of liquid water phase fraction $\gamma = 0.5$ for the case of $\theta_f = 120^\circ$, $\Delta p = 10$ kPa [Colour figure can be viewed at wileyonlinelibrary.com]

initially stagnant in the higher-pressure channel and water emerges from the pore of the GDL bottom.

3.4.1 | Initially side stagnant droplet

Two cases with an initially side stagnant droplet are simulated respectively based on the different hydrophobic GDL ($\theta_f = 90^\circ, 120^\circ$). The case of $\theta_f = 90^\circ$ has been described in Figure 4. Another case of $\theta_f = 120^\circ$ is performed in this section. Figure 9 shows the dynamic behaviors of the side droplet on the surface of the hydrophobic GDL ($\theta_f = 120^\circ$). It is found that the side droplet is unable to flow into the hydrophobic GDL pores and blown out of the flow channel. The reason causing this phenomenon is that the pressure difference $\Delta p_{droplet}$ between the interface of the droplet is too small to outcome the capillary pressure p_c of the small pores of the GDL. The capillary pressure p_c is defined as[40]

$$p_c = p_a - p_w = \frac{4\sigma \cos\theta_f}{d_{pore}} \tag{11}$$

where p_a and p_w are the air and water pressures and d_{pore} and σ are the diameter of GDL pore and the surface tension coefficient of water (exposed to the air).

Taking a pore of $d_{pore} = 80$ μm on the GDL surface as an example, for $\sigma = 0.07$ N m^{-1} and $\theta = 120^\circ$, the absolute capillary pressure p_c of this pore should be 1750 Pa. The

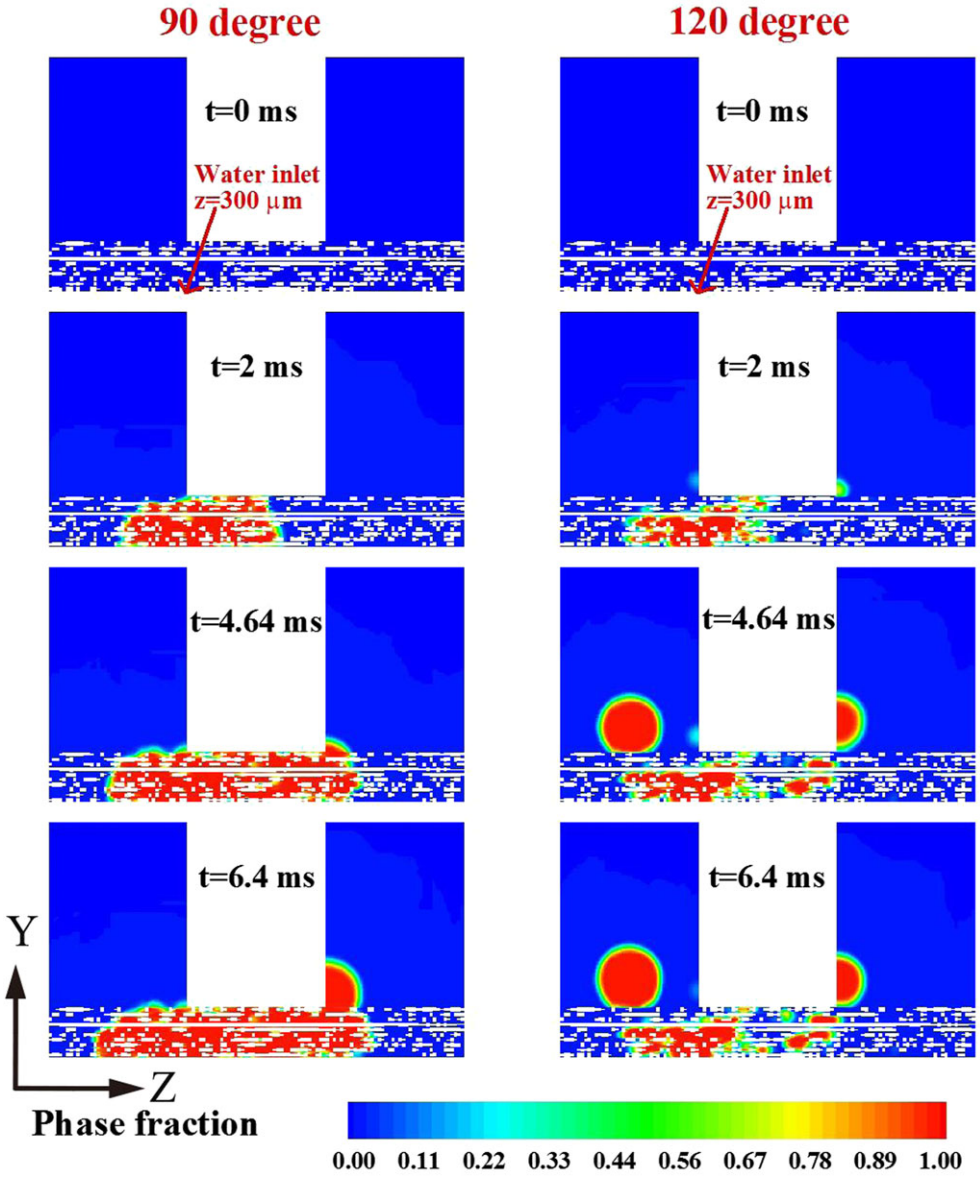

FIGURE 10 Cross flow behaviors of liquid water which initially emerges from the gas diffusion layer (GDL) bottom pore located at $z = 200$ μm (left column: $\theta_f = 90^\circ$, $\Delta p = 7$ kPa; right column: $\theta_f = 120^\circ$, $\Delta p = 7$ kPa) [Colour figure can be viewed at wileyonlinelibrary.com]

maximum of pressure difference Δp_d around the droplet interface is 340 Pa, which is smaller than the capillary pressure. Thus, the droplet in the higher-pressure flow channel cannot be pressed into the hydrophobic GDL under a small pressure difference Δp. It is also noted that the sizes of pores on the GDL surface are nonuniform and have different capillary pressure. As described in Equation 11, when the contact angle is constant, the

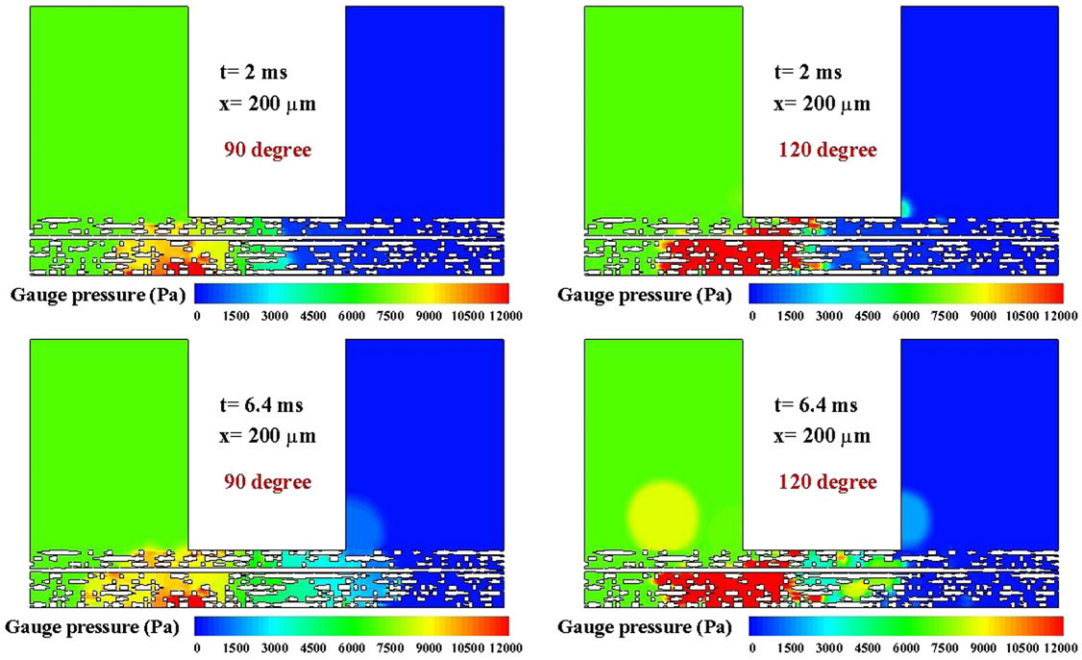

FIGURE 11 Pressure distribution on the slice of $x = 200$ μm at different time instances for the cases of $\theta_f = 90^\circ$ and $\theta_f = 120^\circ$ when water emerging from the pore of the gas diffusion layer (GDL) bottom ($z = 300$ μm) [Colour figure can be viewed at wileyonlinelibrary.com]

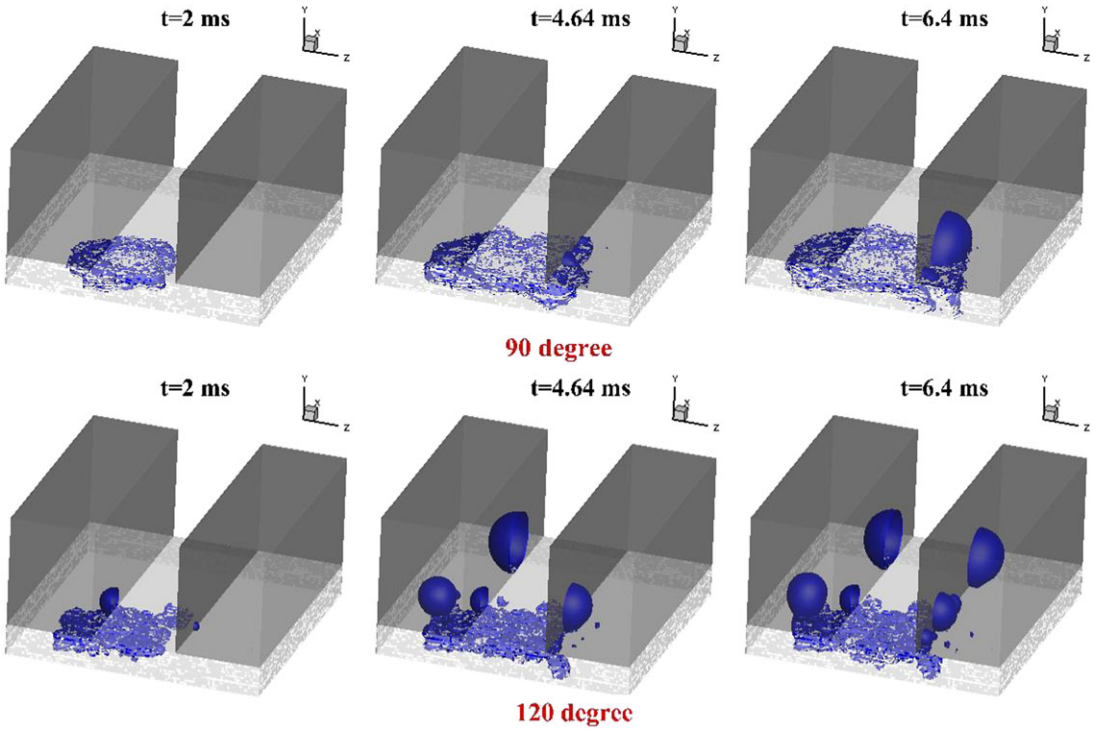

FIGURE 12 Iso-surface of liquid water phase fraction $\gamma = 0.5$ in the process of water emerging from the bottom pores of different hydrophobic GDL (top: $\theta_f = 90^\circ$, $\Delta p = 7$ kPa; bottom: $\theta_f = 120^\circ$, $\Delta p = 7$ kPa) [Colour figure can be viewed at wileyonlinelibrary.com]

smaller pore has larger capillary pressure. For a certain hydrophobic GDL with constant fiber contact angle, when the pressure difference between 2 adjacent channels increases, the droplet will be pressed into large pores firstly.

3.4.2 | Water emerging from bottom pore of gas diffusion layer

The dynamic behaviors of water emerging from the bottom pore of the simulated GDL with different $\theta_f = 90^\circ, 120^\circ$ are simulated in this section. Figure 10 shows the 2D dynamic process of water emerging from a square pore at the GDL bottom (x, z coordinate of the pore is $x = 200$ μm, $z = 300$ μm, respectively). It can be observed that the all the water emerging from the GDL of $\theta_f = 90^\circ$ flows through the under-land GDL and is discharged into the lower-pressure channel completely. While the water emerging from the GDL of $\theta_f = 120^\circ$ partially flows through the under-land GDL and is discharged into lower-pressure channel, most water is discharged into higher-pressure channel directly. The accumulation of water under the higher-pressure channel increases the water pressure and pushes water flowing into the higher-pressure channel, as shown in Figure 11.

Figure 12 shows the iso-surface of liquid water phase fraction $\gamma = 0.5$ in the process of water emerging from the GDL bottom pore. It is seen that liquid water transports along both the x and z directions, indicative of the significant 3D cross flow in GDL and flow channel. For $\theta_f = 120^\circ$, although liquid water emerges under the side wall of the higher-pressure channel ($z = 300$ μm), the liquid water is discharged into the higher-pressure channel through several top locations of the GDL. It is because water accumulation around the pore location results high pressure gradient, which can overcome the capillary resistance between higher-pressure channel and water inlet. It should be noted that section 3.4.1 is to discuss liquid water droplet initially at the GDL surface, while section 3.4.2 focuses on the liquid water emerging from the GDL bottom.

3.4.3 | Summary of two-phase cross flow paths

A diagram of two-phase cross flow paths between 2 adjacent channels is shown in Figure 13. For the GDL of $\theta_f = 90^\circ$, liquid water in the higher-pressure channel mainly takes 2 paths: path 1 (water cross flow between channels) and path 2 (water flow along the channel, from the last higher-pressure channel). Liquid water in the higher-pressure channel is mainly removed through 2 paths: path 1 and path 2. Liquid water emerging in the GDL is removed through path 3 (water enters the neighbor channel).

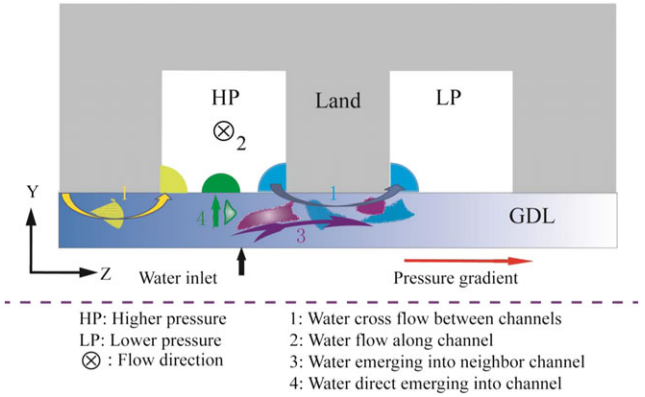

FIGURE 13 Diagram of two-phase cross flow paths [Colour figure can be viewed at wileyonlinelibrary.com]

For the GDL of $\theta_f = 120^\circ$, the liquid water in the higher-pressure channel mainly comes through 2 paths: path 2 and path 4 (water direct emerging into channel). The liquid water in the higher-pressure channel is mainly removed through path 2. The liquid water emerging in the GDL is removed through path 3 and path 4.

3.5 | Effect of pore locations of water emerging

Three different pore locations of water emerging ($z = 150, 300, 450$ μm) are investigated in this section. The schematic of 3 locations is shown in Figure 1. The detailed operating parameters are listed in the Table 1. The case of pore location $z = 300$ μm is previously completed in section 3.4.2. Figure 14 shows the dynamic process of water emerging from different bottom pore locations of the GDL. It can be observed in Figure 14A that most water emerging from the pore location $z = 150$ μm is discharged into the higher-pressure channel; a little water flows through the under-land GDL and is discharged into the lower-pressure channel. When the pore location is set as $z = 300$ μm, nearly a half of the water emerging from the bottom of the GDL is discharged into the lower-pressure channel through the two-phase cross flow effect, which can be observed in Figure 12. Finally, when the pore location is set as $z = 450$ μm, that is, the middle location of the under-land GDL, all of the water emerging from the GDL bottom is discharged into the lower-pressure channel. The direction of pressure difference between 2 adjacent channels and pressure difference between water in GDL and lower-pressure channel contribute similarly to the water removal in GDL. Also,

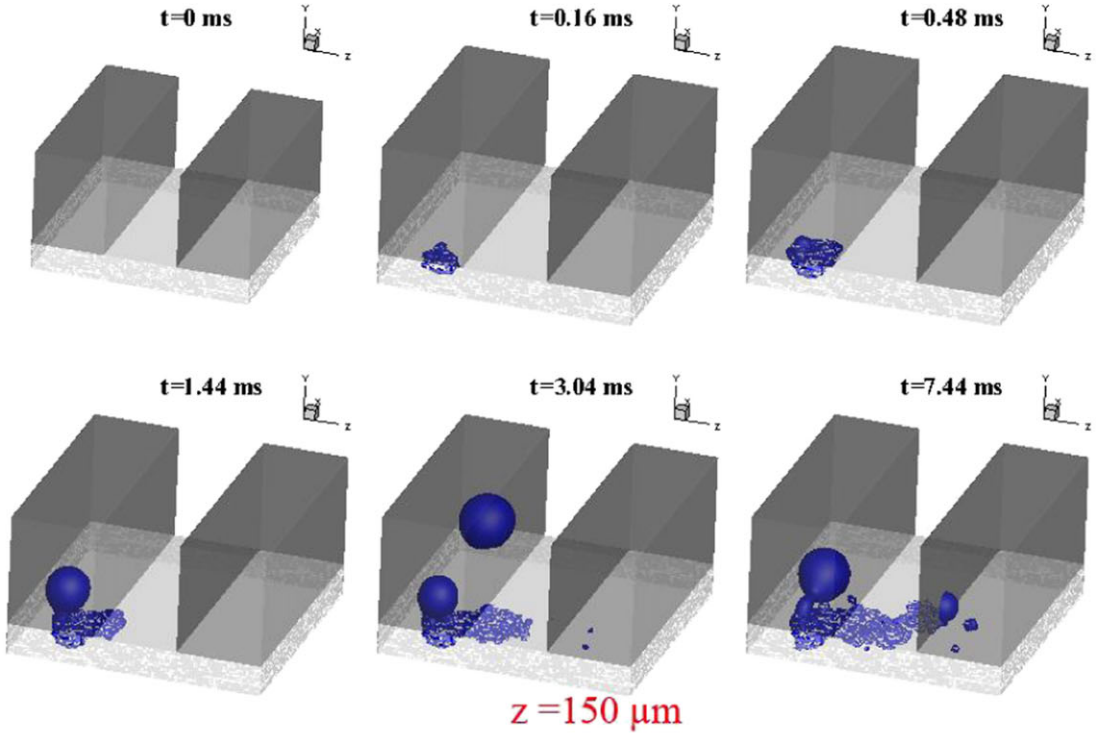

FIGURE 14 Iso-surface of liquid water phase fraction $\gamma = 0.5$ in the process of water emerging from different pores of the gas diffusion layer (GDL) bottom. (A)$z = 150$ μm; (B) $z = 450$ μm. Operating parameters: $\theta_f = 120°$, $\Delta p = 7$ kPa [Colour figure can be viewed at wileyonlinelibrary.com]

both the pressure difference between 2 adjacent channels and capillary pressure hinder the water flow toward the higher-pressure channel. Thus, it can be concluded that water emerging from the location near the lower-pressure channel is easier to be removed into lower-pressure channel by cross flow.

4 | CONCLUSION

In this study, a 3D VOF model was developed and applied to study the two-phase cross flow in the GDL under a land. The effects of the GDL pore structures on the two-phase cross flow were considered by reconstructing the morphology GDL by using the stochastic method. The validation of the reconstructed GDL was confirmed by comparing its gas permeability with the value obtained from the TS model. It is found that the corner droplet in the higher-pressure channel was easier to remove via the GDL for a contact angle $\theta_f = 90^\circ$ by cross flow than droplet at other locations. The droplet could not be forced into the GDL when the GDL is more hydrophobic ($\theta_f = 120^\circ$) because of the significant capillary effect. In the GDL of $\theta_f = 90^\circ$, liquid water emerging from the GDL bottom in the higher-pressure channel side was dragged by the air cross flow to the lower-pressure channel via the under-land GDL. For the hydrophobic GDL ($\theta_f = 120^\circ$), part of liquid water emerging from the GDL bottom was also removed to the higher-pressure channel as well due to the capillary action. A diagram of two-phase cross flow paths was developed to illustrate the possible liquid water paths. Finally, it was found that liquid water emerging from the GDL bottom near the lower-pressure channel is easier to be removed to the lower-pressure channel by cross flow, as expected.

ACKNOWLEDGEMENTS

This research is supported by the National Key Research and Development Program of China (grant no 2016YFB0101303).

ORCID

Kui Jiao http://orcid.org/0000-0002-1296-1330

REFERENCES

1. Chang D, Wu S. The effects of channel depth on the performance of miniature proton exchange membrane fuel cells with serpentine-type flow fields. *Int J Hydrogen Energy*. 2015;40:11,659-11,667.
2. Yang W, Wang H, Kim Y. Effects of the humidity and the land ratio of channel and rib in the serpentine three-dimensional PEMFC model. *Int J Energy Res*. 2013;37:1339-1348.
3. Su A, Chiu Y, Weng F. The impact of flow field pattern on concentration and performance in PEMFC. *Int J Energy Res*. 2005;29:409-425.
4. Gibson C, Meybodi M, Behnia M. A methodology to compare the economic feasibility of fuel cell-, gas turbine- and microturbine-based combined heat and power systems. *Int J Energy Res*. 2008;40:983-1008.
5. Wang Y, Basu S, Wang C. Modeling two-phase flow in PEM fuel cell channels. *J Power Sources*. 2008;179:603-617.
6. Cooper N, Santamaria A, Becton M, Park J. Investigation of the performance improvement in decreasing aspect ratio interdigitated flow field PEMFCs. *Energ Conver Manage*. 2017;136:307-317.
7. Park J, Li X. An analytical analysis on the cross flow in a PEM fuel cell with serpentine flow channel. *Int J Energy Res*. 2011;35:583-593.
8. Wang Y, Wang C. Simulations of flow and transport phenomena in a polymer electrolyte fuel cell under low-humidity operations. *J Power Source*. 2011;147:148-161.
9. Bachman J, Santamaria A, Tang H, Park J. Investigation of polymer electrolyte membrane fuel cell parallel flow field with induced cross flow. *J Power Sources*. 2012;198:143-148.
10. Jiao K, Bachman J, Zhou Y, Park J. Effect of induced cross flow on flow pattern and performance of proton exchange membrane fuel cell. *Appl Energy*. 2014;115:75-82.
11. Jiao K, Park J, Li X. Experimental investigations on liquid water removal from the gas diffusion layer by reactant flow in a PEM fuel cell. *Appl Energy*. 2010;87:2770-2777.
12. Shah M, Kandlikar S. Water emergence from the land region and water sidewall interactions in proton exchange membrane fuel cell gas channels with microgrooves. *J Power Sources*. 2015;297:127-139.
13. Spernjak D, Prasad A, Advani S. In situ comparison of water content and dynamics in parallel, single-serpentine, and interdigitated flow fields of polymer electrolyte membrane fuel cells. *J Power Sources*. 2011;195:3553-3568.
14. Tabe Y, Lee Y, Chikahisa T, Kozakai M. Numerical simulation of liquid water and gas flow in a channel and a simplified gas diffusion layer model of polymer electrolyte membrane fuel cells using the lattice Boltzmann method. *J Power Sources*. 2009;193:24-31.
15. Chen L, Luan H, He Y, Tao W. Pore-scale flow and mass transport in gas diffusion layer of proton exchange membrane fuel cell with interdigitated flow fields. *Int J Therm Sci*. 2012;51:132-144.
16. Palakurthi N, Konangi S, Ghia U, Comer K. Micro-scale simulation of unidirectional capillary transport of wetting liquid through 3D fibrous porous media: estimation of effective pore radii. *Int J Multiphase Flow*. 2015;77:48-57.
17. Liu Z, Wu H. Pore-scale modeling of immiscible two-phase flow in complex porous media. *Appl Therm Eng*. 2016;93:1394-1402.
18. Ferreira R, Falcao D, Oliveria V, Pinto A. Numerical simulations of two-phase flow in proton exchange membrane fuel cells using the volume of fluid method—a review. *J Power Sources*. 2015;277:329-342.
19. Suresh P, Jayanti S. Effect of air flow on liquid water transport through a hydrophobic gas diffusion layer of a polymer electrolyte membrane fuel cell. *Int J Hydrogen Energy*. 2010;35:6872-6886.

20. Park J, Jiao K, Li X. Numerical investigations on liquid water removal from the porous gas diffusion layer by reactant flow. *Appl Energy*. 2010;87:2180-2186.
21. Yin Y, Wu T, He P, Du Q, Jiao K. Numerical simulation of two-phase cross flow in microstructure of gas diffusion layer with variable contact angle. *Int J Hydrogen Energy*. 2014;39:15,772-15,785.
22. Hao L, Cheng P. Lattice Boltzmann simulations of water transport in gas diffusion layer of a polymer electrolyte membrane fuel cell. *J Power Sources*. 2010;195:3870-3881.
23. Gao Y, Zhang X, Rama P, Chen R, Ostadi H, Jiang K. Lattice Boltzmann simulation of water and gas flow in porous gas diffusion layers in fuel cells reconstructed from micro-tomography. *Comput Math Appl*. 2013;65:891-900.
24. Bednarek T, Tsotridis G. Calculation of effective transport properties of partially saturated gas diffusion layers. *J Power Sources*. 2017;340:111-120.
25. Jeon D, Kim H. Effect of compression on water transport in gas diffusion layer of polymer electrolyte membrane fuel cell using lattice Boltzmann method. *J Power Sources*. 2015;294:393-405.
26. Sung C, Wang Y, Chen K. Droplet dynamics in a polymer electrolyte fuel cell gas flow channel: forces, deformation and detachment. II: comparisons of analytical solution with numerical and experimental results. *J Power Sources*. 2012;210:191-197.
27. Schulz V, Becker J, Wiegmann A, Mukherjee P, Wang C. Modeling of two-phase behavior in the gas diffusion medium of PEFCs via full morphology approach. *J Electrochem Soc*. 2007;154:B419-B426.
28. Inoue G, Yoshimoto T, Matsukuma Y, Minemoto M. Development of simulated gas diffusion layer of polymer electrolyte fuel cells and evaluation of its structure. *J Power Sources*. 2008;175:145-158.
29. Hao L, Cheng P. Lattice Boltzmann simulations of anisotropic permeabilities in carbon paper gas diffusion layers. *J Power Sources*. 2009;186:104-114.
30. Nada Z, Li X, Shen J. Numerical estimation of the effective electrical conductivity in carbon paper diffusion media. *Appl Energy*. 2012;93:39-44.
31. Litster S, Sinton D, Djilali N. Ex situ visualization of fluid water transport in PEM fuel cell gas diffusion layers. *J Power Sources*. 2006;154:95-105.
32. Wang Y, Chen K, Mishler J, Cho SC, Adroher XC. A review of polymer electrolyte membrane fuel cells: technology, applications, and needs on fundamental research. *Appl Energy*. 2011;88:981-1007.
33. Berberovic E, Hinsberg N, Jakirlic S, Roisman I, Tropea C. Drop impact onto a liquid layer of finite thickness: dynamics of the cavity evolution. *Phys Rev E*. 2009;79:036306
34. Harting C, Manke I, Kuhn R, Kleinau S, Goebbels J, Banhart J. High-resolution in-plane investigation of the water evolution and transport in PEM fuel cells. *J Power Sources*. 2009;188:468-474.
35. Tomadakis M, Robertson T. Viscous permeability of random fiber structures: comparison of electrical and diffusional estimates with experimental and analytical results. *J Compos Mater*. 2005;39:163-188.
36. Owejan JP, Trabold TA, Jacobson DL, Baker DR, Hussey DS, Arif M. In situ investigation of water transport in an operating PEM fuel cell using neutron radiography: part 2—transient water accumulation in an interdigitated cathode flow field. *Int J Heat Mass Tran*. 2006;49:4721-4731.
37. Jiao K, Park JW, Li XG. Experimental investigations on liquid water removal from the gas diffusion layer by reactant flow in a PEM fuel cell. *Appl Energy*. 2010;87:2770-2777.
38. Jiao K, Bachman J, Zhou YB, Park JW. Effect of induced cross flow on flow pattern and performance of proton exchange membrane fuel cell. *Appl Energy*. 2014;115:75-82.
39. Hsieh SS, Her BS, Huang YJ. Effect of pressure drop in different flow fields on water accumulation and current distribution for a micro PEM fuel cell. *Energ Conver Manage*. 2011;52:975-982.
40. Jiao K, Li XG. Water transport in polymer electrolyte membrane fuel cells. *Progr Energy Combust Sci*. 2011;37:221-291.

How to cite this article: Niu Z, Jiao K, Wang Y, Du Q, Yin Y. Numerical simulation of two-phase cross flow in the gas diffusion layer microstructure of proton exchange membrane fuel cells. *Int J Energy Res*. 2018;42:802–816. https://doi.org/10.1002/er.3867